Distance Distributions of Photogenerated Charge Pairs in Organic Photovoltaic Cells

Alex J. Barker, Kai Chen, and Justin M. Hodgkiss*

The MacDiarmid Institute for Advanced Materials and Nanotechnology, Wellington 6140, New Zealand

School of Chemical and Physical Sciences, Victoria University of Wellington, Wellington 6010, New Zealand

S *Supporting Information*

ABSTRACT: Strong Coulomb interactions in organic photovoltaic cells dictate that charges must separate over relatively long distances in order to circumvent geminate recombination and produce photocurrent. In this article, we measure the distance distributions of thermalized charge pairs by accessing a regime at low temperature where charge pairs are frozen out following the primary charge separation step and recombine monomolecularly via tunneling. The exponential attenuation of tunneling rate with distance provides a sensitive probe of the distance distribution of primary charge pairs, reminiscent of electron transfer studies in proteins. By fitting recombination dynamics to distributions of recombination rates, we identified populations of charge-transfer states and well-separated charge pairs. For the wide range of materials we studied, the yield of separated charges in the tunneling regime is strongly correlated with the yield of free charges measured via their intensity-dependent bimolecular recombination dynamics at room temperature. We therefore conclude that populations of free charges are established via long-range charge separation within the thermalization time scale, thus invoking early branching between free and bound charges across an energetic barrier. Subject to assumed values of the electron tunneling attenuation constant, we estimate critical charge separation distances of ∼3−4 nm in all materials. In some blends, large fullerene crystals can enhance charge separation yields; however, the important role of the polymers is also highlighted in blends that achieved significant charge separation with minimal fullerene concentration. We expect that our approach of isolating the intrinsic properties of primary charge pairs will be of considerable value in guiding new material development and testing the validity of proposed mechanisms for long-range charge separation.
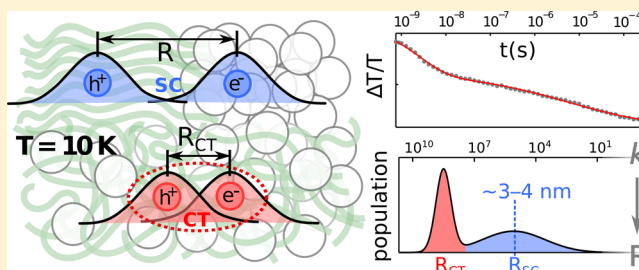
■ INTRODUCTION

Rational design of effective organic photovoltaic (OPV) materials requires understanding how interfacial charge pairs achieve sufficient separation to overcome their mutual Coulombic attraction. Simple application of Coulomb's law suggests that in a medium with a dielectric constant of ∼3.5, point charges must achieve a separation of ∼4 nm before their interaction energy is less than the intrinsic energetic disorder of typical organic materials (0.1 eV).[1−3] Entropic considerations and charge delocalization will favor charge separation, nevertheless, charge pairs that fail to separate by more than a few nanometers are likely to collapse into tightly bound charge-transfer (CT) states and recombine monomolecularly, often radiatively.[4−11] The observed sensitivity of OPV device efficiency to blend morphology[12,13] can be attributed to the need for donor and acceptor phases to be large enough to support formation of separated charges (SCs); blends that are too finely intermixed result in terminal CT states forming at the expense of extractable free charges.[6,9,14,15]

Several compelling models for free charge photogeneration have emerged from recent experimental observations and modeling. Onsager-type models describe direct branching between bound CT states and free charges via hot CT states that can thermalize at charge pair distances exceeding thermal capture, possibly benefiting transiently from delocalization.[1,2,16−20] Direct branching is evidenced by CT states that can only contribute photocurrent when re-excited[16] and via kinetic modeling of recombination dynamics.[9] On the other hand, the role of excess energy is disputed via the observation of photocurrent quantum efficiencies that are independent of excitation energy,[21] including for direct excitation of thermalized CT states when the CT absorption spectrum is inferred via electroluminescence spectra.[22] It has further been proposed that the broadened density of states associated with disorder leads to extremely high (non-equilibrium) initial charge carrier mobilities that are sufficient for charge pairs to rapidly diffuse apart on thermalization time scales,[23,24] or that excitons can be dissociated at long range from interfaces.[25] In spite of the emergence of models describing different relationships between excitons, CT states and SCs on a potential energy surface spanning several nanometers from the donor/acceptor interface, critical parameters including distances have yet to be experimentally established.

Measured phase sizes from optimized blends provide some guidance on critical length scales for interfacial charge separation; however, phase optimization is also coupled to exciton transport and charge extraction processes. Direct spectroscopic probes of distances are challenging because only radiatively coupled CT states provide optically distinct emissive signatures that identify them as tightly bound.[8,26–28] More widely observed polaron absorption signatures are generally insensitive to the proximity of other charges.

Several recent attempts to resolve dynamics of charge pair distances have targeted phenomena that depend on the electric field created by charge separation. Time-resolved second harmonic generation spectroscopy has been used to resolve photovoltage generation on various time scales; however, symmetry requirements restrict the technique to in planar bilayer devices.[19,29,30] Electroabsorption (Stark shift) effects are observed in dye-sensitized[31] and organic bulk heterojunction photovoltaic devices.[17] Their magnitude can be related to charge pair distances, leading to critical distances on the order of 4 nm for efficient OPVs;[17] however, this analysis requires that optically active components have a very sharp absorption edge so that the derivative-like electroabsorption features can be clearly identified and extracted from overlapping polaron, bleaching, and stimulated emission features. Finally, simultaneous measurements of dielectric and electron spin resonance susceptibilities for OPVs revealed ~4 nm charge localization lengths at cryogenic temperatures.[32]

Here, we present a new approach for determining the distance distribution of initially thermalized charge pairs. At low temperature, we are able to access a regime, previously identified in neat polymer films,[33] where all charge pairs are effectively frozen following the primary charge separation step and recombine slowly via monomolecular tunneling. The exponential distance dependence of tunneling provides a sensitive probe of the distance distribution of initial charge pairs. For the wide range of OPV blends we probed, we find that dynamics are well fit to a bimodal distribution of tunneling recombination rates, consistent with branching between populations of CT states and SCs within the thermalization time scale. We observe a universal link between the free charge yield measured at room temperature and the yield of SCs frozen at low temperature. Our measurements confirm that free charge yields are established via the charge pairs that achieve an estimated ~3−4 nm separation within the thermalization time scale. We also resolve the effect of polymer and fullerene components on the primary charge separation step.

EXPERIMENTAL DETAILS

All materials were commercially sourced and spin-coated onto spectrosil fused silica substrates as described in the Supporting Information. All samples were measured under dynamic vacuum and, where indicated, cooled to 10 K by a closed-cycle helium cryostat (CTI-Cryogenics).

Charge recombination was measured via transient absorption (TA) spectroscopy, in which 532 (or 355) nm excitation pulses were generated from the second (or third) harmonic of a Q-switched Nd:YVO$_4$ laser (AOT-YVO-25QSP, 700 ps) and filtered to the fluences indicated. The 700 ps excitation pulsewidth defines the experimental time resolution. A portion of the 800 nm output of an amplified Ti-sapphire (Spectra-Physics Spitfire, 100 fs, 3 kHz) was used as a probe after splitting to introduce a reference channel for improved signal sensitivity. The transmitted probe light was spectrally dispersed using a fiber-coupled spectrograph (Princeton Instruments SP150) and read out at 3 kHz using a dual-channel linear photodiode

array (Stresing). The pump−probe delay was electronically varied out to 300 μs by a delay generator (Stanford Systems, DG535). Additional measurements of fast recombination in poly[2-methoxy-5-(2-ethyl-hexyloxy)-1,4-phenylenevinylene] (MEH-PPV):phenyl-C$_{61}$-butyric acid methyl ester (PCBM) blends used the 100 fs, 532 nm output of a parametric amplifier (TOPAS) as an excitation source, with the pump−probe delay varied by use of a retroreflector mounted on a motorized delay stage with time resolution of ~100 fs and delay range of ~2 ns. Approximately 10 000 shot pairs were averaged for each time point and repeated over ~20 scans. Some variation was needed to account for signal strength at different intensities. The signal strength was found to vary by <5% between the first and last scans with no discernible trend, verifying that negligible photo-degradation occurred during the measurements.

Data fitting was carried out in MATLAB (MathWorks), using the Nelder−Mead algorithm to minimize the sum of squares of the deviation between the measured data and the tunneling and intensity-dependent decay models described. For both models, four parameters were fitted, and equal weighting was given to each order of magnitude of pump−probe delay.

RESULTS AND DISCUSSION

Charge Recombination at Low Temperature. Our approach to measuring photogenerated charge pair distances requires accessing a regime where even SCs are frozen and slowly recombine monomolecularly via tunneling. It is well known that the preceding charge photogeneration step is not impeded at low temperature because excitons have sufficient excess thermal energy to reach interfaces before they relax.[20,34,35] Figure 1 presents several independent verifications that we can access the monomolecular tunneling recombination regime.
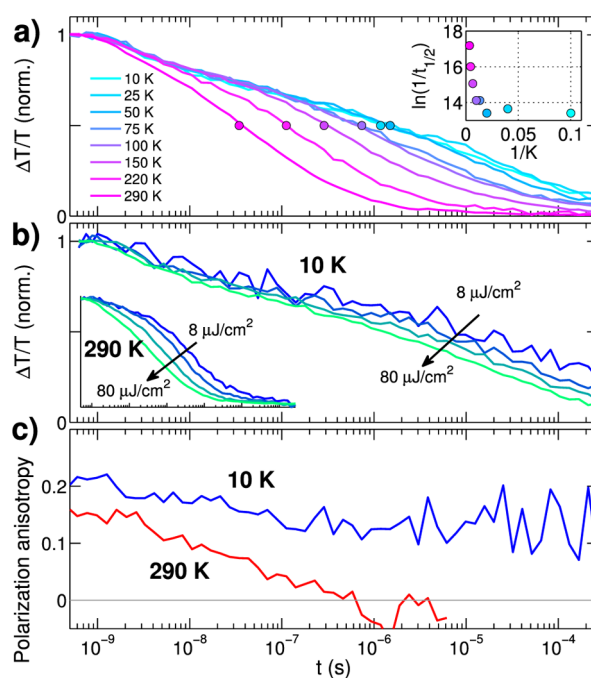
Figure 1. Recombination dynamics for a vapor annealed P3HT:PCBM blend film excited at 532 nm and probed at 800 nm. (a) Temperature-dependent recombination (80 μJ/cm^2 excitation), with corresponding $t_{1/2}$ values represented in an Arrhenius-type plot in the inset. (b) Intensity-dependent recombination for the same film at 10 and 290 K. (c) Polarization anisotropy decay for the same film measured at 10 and 290 K, 16 μJ/cm^2 excitation.

Figure 1a shows the temperature-dependent charge recombination dynamics for a vapor annealed regioregular poly(3-hexylthiophene) (P3HT):PCBM blend film, probed via the polymer hole polaron absorption signature in the near IR.[6,9,14,36] The probed time range commences beyond that of exciton dynamics. Excitons (including potentially triplet excitons) and charges are clearly distinguished in the infrared.[6,37] We carried out additional measurements with broadband IR (830–1600 nm) and visible (530–850 nm) probes for fs–μs and fs–ns time scales, respectively (see Supporting Information). These measurements allowed us to confirm that only charges are present on the ns–μs range studied here, and the charge population can be probed with 800 nm pulses, which has the additional benefit of exceptional sensitivity. We note that the precedence for triplet exciton formation in P3HT relates only to solution measurements[38,39] or films of disordered regiorandom P3HT in the absence of the PCBM quencher.[37]

The time range probed in Figure 1 captures recombination of virtually the entire charge population. At 290 K, bimolecular recombination dominates due to the high yield of free (mobile) charges photogenerated, as evidenced by the strongly intensity-dependent 290 K recombination dynamics in Figure 1b (inset).[9] This behavior typifies the active layer of an efficient OPV device except that in devices, free charges are extracted by the electrodes in competition with bimolecular charge recombination.[40] In the bimolecular recombination regime, recombination dynamics are non-geminate and do not directly reflect the properties of initially photogenerated charge pairs. As the temperature decreases, recombination slows and below ∼50 K, we observe a temperature-independent regime of activationless charge recombination. The observed transition temperature is similar to previous observations of recombination in neat P3HT films owing to the intrinsic polymer-based activation barrier for polaron hopping in semiconducting polymers.[33] It is worth noting that cooling to only 77 K (readily accessible with nitrogen cryostats) is insufficient to freeze charge motion, consistent with the observation by Mauer et al. of functioning devices and intensity-dependent recombination at 80 K.[41] Figure 1b shows that the distinctive intensity dependence observed at 290 K (inset) is largely lost at 10 K since bimolecular charge recombination is thermally shut off. Instead, the predominantly monomolecular decay is attributed to charges being thermally trapped as geminate charge pairs near the site of their initial generation. Thus, charge pairs that would otherwise be free at room temperature remain frozen as SCs at low temperature. The residual weak intensity dependence at high intensity may result from charge delocalization at low temperature.[32] Finally, the weak polarization anisotropy decay shown in Figure 1c confirms that charges are effectively immobile at 10 K, in contrast to the complete loss of polarization anisotropy associated with mobile charges at 290 K.

To summarize this section, the temperature-, intensity-, and polarization-resolved TA measurements in Figure 1 verify that below 50 K, charge pairs are effectively immobile beyond the thermalization time scale, leading to eventual monomolecular recombination, even for SCs.

Tunneling Recombination and Distance Distributions.
The Arrhenius-type plot in Figure 1a (inset) is reminiscent of DeVault and Chance's renowned observation of temperature-independent electron transfer (ET) in photosynthetic proteins at low temperature.[42,43] Their experiment stimulated theoretical

efforts to put Marcus theory into a quantum mechanical framework to describe long-range electron tunneling mediated by quantum modes.[44,45] In the low temperature regime, when quantum modes are not thermally accessible, the rate of ET is most sensitive to the donor–acceptor electronic coupling, V_{DA}, assuming coupling between donor and acceptor states of the same energy. V_{DA} is exponentially dependent on distance owing to the exponential character of wave functions in the tunneling region,

$$V_{DA} = V_0 \exp\left(\frac{-\beta(R_{DA} - R_0)}{2}\right) \qquad (1)$$

Here, the electronic coupling at a given donor–acceptor distance, R, is referenced to the coupling, V_0, at a distance of R_0. The scaling factor, β, describes the rate of attenuation with distance. Assuming negligible distance dependence in other terms aside from V_{DA}, the distance dependence of the electron transfer rate from donor to acceptor, k_{DA}, is

$$k_{DA} = k_0 \exp(-\beta(R_{DA} - R_0)) \qquad (2)$$

Extensive measurements in proteins featuring redox labels at well-defined distances have revealed β values on the order of 1 Å^{-1} for ET rates spanning many orders of magnitude.[46] Well-defined molecular donor–bridge–acceptor complexes have also firmly established the sensitivity of ET rates to distance according to eq 2.[47]

With this is mind, we set about using measured charge recombination rates in the tunneling regime as a probe of charge pair separations. By rearranging eq 2, we see that it is not necessary to fully account for absolute ET rates (in this case charge recombination) because the distance distribution is obtained from relative recombination rates for charge pairs in the same material blend:

$$-\ln\left(\frac{k}{k_{CT}}\right) = \beta(R - R_{CT}) \qquad (3)$$

Provided that we resolve a fast recombination component that can be attributed to bound CT states (presumably with an electron–hole separation $R_{CT} \approx 0.5$–1 nm), all slower recombination rate constants (k) can be referenced to k_{CT}. According to eq 3, we can use the observed rates to extract charge pair separation, R, relative to the reference distance R_{CT}, as depicted in Scheme 1. We note that our use of the term CT state here refers only the fastest recombination rates (closest distances), rather than identification of radiative coupling, as per the formal definition of CT states. The absolute distance scale is set by the value of β, which we will return to later.

Figure 2 shows the tunneling recombination dynamics for a P3HT:PCBM blend film at 10 K. Although we have accessed a sufficiently low temperature for charge recombination to be predominantly monomolecular, the decay in Figure 2 clearly cannot be fit with a monoexponential or even biexponential decay. Most of the observed recombination is highly dispersive, which is not surprising for a disordered bulk heterojunction blend and reflects a distribution of charge pair separations. We are therefore forced to fit to a distribution of rate constants spanning the wide range of time scales observed.

By observing how closely simple distributions of rate constants fit the experimental decay in Figure 2, we are guided toward a model that captures the data with minimal free parameters. The charge recombination dynamics appear to be

Scheme 1. Obtaining Charge Pair Distance from Tunneling Recombination Dynamics
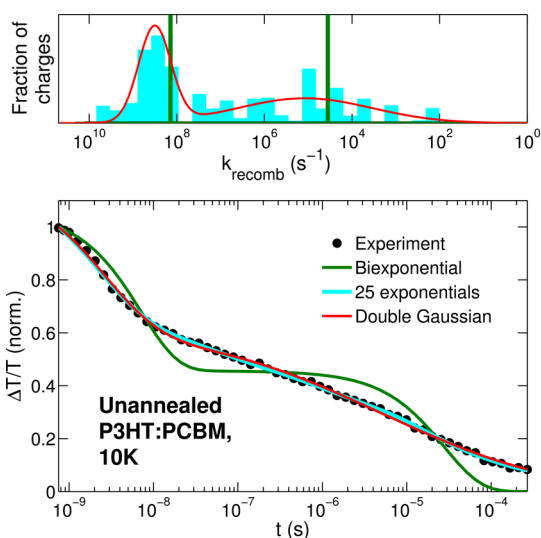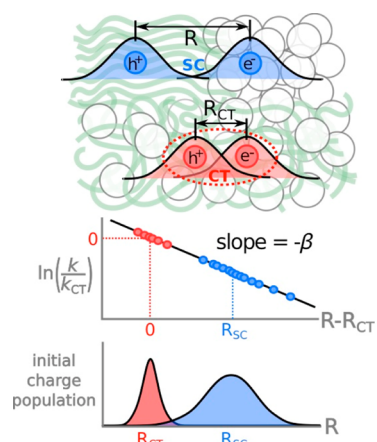

Figure 2. 10 K recombination dynamics for an unannealed P3HT:PCBM film fit to various possible distributions of exponential decay functions. The corresponding rate constant distributions are shown in the top panel.

described by a rapid early (<10 ns) phase that may be fit by a narrow distribution of rate constants, followed by slower dynamics that clearly demand a much broader distribution of rate constants. An excellent fit to the experimental decay was achieved using a series of logarithmically distributed rate constants with unconstrained amplitudes. It can be seen that a bimodal rate distribution emerges after initialization with a flat distribution. Since the experiment spans a wide enough time window to resolve the decay of the entire charge population, and the basis rate constants span a large range, we are assured that the emergence of bimodality is not an artifact of sampling. We will return later to the physical implications of a bimodal rate distribution. Nevertheless, in spite of the fit quality, the excess parameters in the unconstrained fit impair quantitative comparison between samples. Balancing the requirements to fit a bimodal rate distribution with minimal free parameters led us to fit to a rate distribution reflecting a double Gaussian charge pair distance distribution (i.e., double Gaussian on a logarithmic rate scale). Further attempted fitting possibilities are shown in the Supporting Information.

Figure 2 confirms that with two Gaussians, we achieve an excellent fit to the experimental data. The fit is not unique; many other bimodal functions could fit the highly dispersive decays equally well, as the unconstrained distribution in Figure 2 illustrates. However, the Gaussian model does so with minimal free parameters, from which physically meaningful insights can be derived. The unconstrained fit with 25 independent exponentials in Figure 2 suggests that the faster phase should fit to a relatively narrow distribution of rate constants; therefore, we fixed its width to $k_{CT,fwhm} = 2$. Thus, we are left with only four free parameters: the two peak positions, their amplitude ratio, and the width of slower peak. Fixing the width of the fast component decreases the fitting error associated with its position, ensuring that the fast component taken to represent the reference k_{CT} is well anchored. The two Gaussian rate constant distributions that best fit the data are peaked around 3×10^8 and 1×10^5 s^{-1}, integrating to account for 48% and 52% of the total charge population, respectively. Our simple model therefore provides a simple measure of the yields of CT states and SCs.

Free Charges at Room Temperature vs Low Temperature. Although the observed bimodal recombination rate distributions may be affected by differences in geometric factors, we consider distance to be of primary importance. In this interpretation, the bimodal rate distribution implies separate populations of closely bound CT states and SCs that would otherwise be free at room temperature. The ~3 ns lifetime associated with the peak of the fast Gaussian component (defined as k_{CT}) is in line with expectations for bound CT states in P3HT:PCBM blends, where 2−4 ns lifetimes are found at room temperature.[9] Second, the relative yields of the two populations closely matches the relative yields of bound versus free charges measured independently for the same samples via intensity-dependent recombination kinetics at room temperature. Here, we apply the model introduced by Howard et al.,[9] whereby the total decay is described by two populations formed via an ultrafast branching step; bound CT states recombine monomolecularly with a fixed rate, and free charges undergo intensity-dependent non-geminate recombination, where the order close to two indicates bimolecular character. A common set of four parameters are globally fit across a wide range of intensities: branching ratio, monomolecular and non-geminate rate constants, and non-geminate recombination order. The fitted branching ratio is a robust measure of free charge photogeneration yield that correlates well with device quantum efficiency at room temperature. Figure 3c shows the room-temperature intensity-dependent recombination dynamics for the unannealed P3HT:PCBM film. The fitted 59% free charge photogeneration efficiency closely matches the 52% SC yield associated with slower Gaussian component.

In order to test our interpretation that the slow Gaussian component reflects frozen SCs that would otherwise be free at room temperature, we investigated the effect of solvent vapor annealing. Annealing is known to produce blend morphologies that lead to higher free charge yields.[48] Figure 3b shows that solvent vapor annealing leads to slower 10 K charge recombination dynamics. When applying the fit, both Gaussian components undergo negligible shifts in peak rate constants, rather a higher weight (71%), in the slow Gaussian component accounts for the slower dynamics. The result of the fit is reasonable since the main effect of annealing on the raw recombination data is clearly in the relative weightings of fast
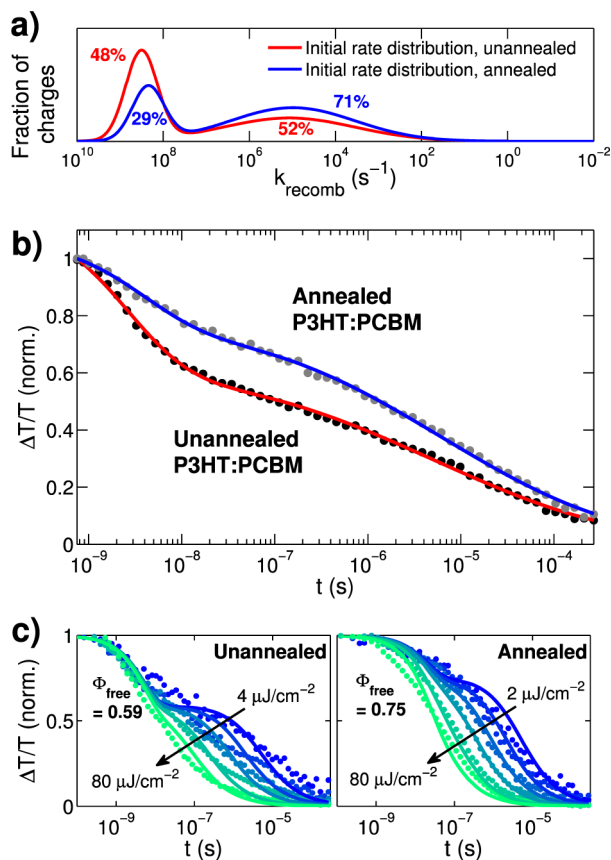
Figure 3. (a) Double Gaussian distribution of rate constants used to fit recombination decay in (b) for annealed and vapor unannealed P3HT:PCBM blend films at 10 K. (c) Room-temperature intensity-dependent recombination for the same films fitted to the kinetic model presented in ref 9.

(<10 ns) and slower recombination phases. Again, the relative yield of SCs follows the increased yield of free charges measured via intensity-dependent recombination kinetics at room temperature (75%, Figure 3c).

Recombination in Various Polymer:Fullerene Blends. Having established that we are able to identify SCs via their recombination dynamics at 10 K, we applied the procedure to a range of other polymer:fullerene blends of varying efficiency in order to interrogate whether a universal correlation exists. Our survey included low bandgap polymers poly[N-9′-hepta-decanyl-2,7-carbazole-alt-5,5-(4′,7′-di-2-thienyl-2′,1′,3′-benzo-thiadiazole)] (PCDTBT) and poly[2,6-(4,4-bis(2-ethylhexyl)-4H-cyclopenta[2,1-b;3,4-b″]dithiophene)-alt-4,7-(2,1,3-benzo-thiadiazole)] (PCPDTBT), along with MEH-PPV. We also investigated the effect of blend ratio and excitation wavelength in order to distinguish the role of polymer and fullerene phases in free charge photogeneration. Unless otherwise stated, for each film we measured both recombination dynamics at 10 K, as well as intensity-dependent recombination dynamics at 290 K. Each sample was probed at 800 nm, which in most cases corresponds to photoinduced absorption due to the hole polaron population. The exception is the PCPDTBT blend, for which the signal at 800 nm tracks the ground-state bleach recovery, which is proportional to charge density on the time scales studied here. Again, the benefit of using an 800 nm probe is that its superior stability permits exceptional signal sensitivity, which is crucial for low excitation fluence measurements.

Broadband visible and IR TA spectra for each blend (see Supporting Information) verify that 800 nm is a valid wavelength to probe charge recombination. In particular, the spectral features from charges extending into the IR on the early nanosecond time scale do not exhibit subsequent spectral shifts on longer time scales, allowing us to rule out recombination to triplet exciton states and justifying a single wavelength probe. In spite of the documented similarity of charge and triplet PIA features around 1300 nm in PCPDTBT,[49,50] the signature bimolecular recombination we observe at room temperature (Supporting Information) is evidence that our film morphology strongly favors charges over triplets, in line with Etzold et al.[50] Particularly fast recombination in MEH-PPV:PCBM blends required the use of a femtosecond excitation source to resolve the signal from 10^{-11} to 10^{-9} s. The Supporting Information describes how these data were scaled to overlap with the long-delay data set.

Figure 4 shows the set of recombination dynamics at 10 K along with the fitted distributions of recombination rate
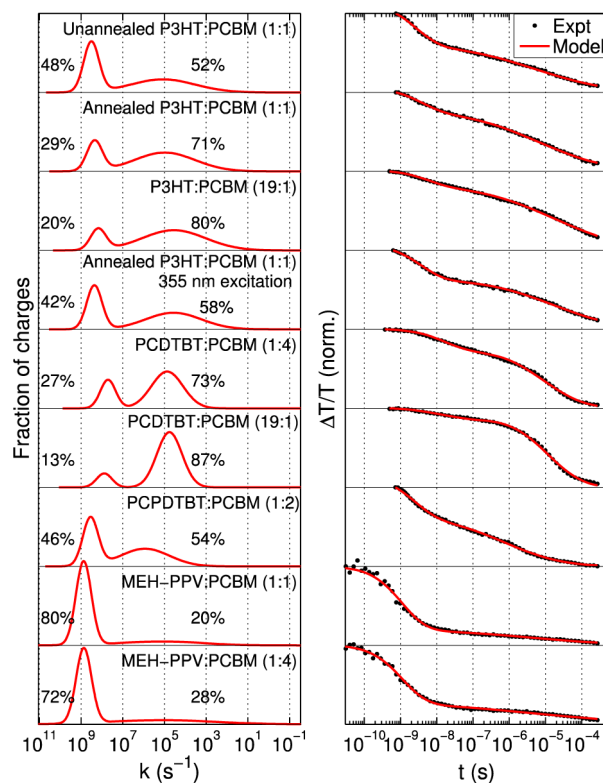
Figure 4. 10 K charge recombination dynamics (right) for various blend films and the corresponding distributions of rate constants (left) used to fit the decays. The relative yields contained in each Gaussian component are indicated on the plots. Alternative unconstrained rate distributions for each sample are provided in the Supporting Information. Unless otherwise stated, samples were photoexcited at 532 nm (~40 μJ/cm^2) and probed at 800 nm. For data at short time delay (10^{-11}–10^{-9} s), MEH-PPV:PCBM was photoexcited at 532 nm (12 μJ/cm^2, 100 fs).

constants. The P3HT:PCBM data from Figure 3 are repeated here for ease of comparison. Key fitting parameters, along with the yield of free charges independently fitted via intensity-dependent recombination at 290 K (Supporting Information) are summarized in Table 1. Figure 4 demonstrates that the double Gaussian model produces excellent fits of the observed

Table 1. Fitting Parameters for Charge Recombination Measurements in Different Blend Films

sample	$k_{CT}{}^{a}/$ 10^8 s^{-1}	$k_{SC}{}^{b}/$ 10^4 s^{-1}	$-\ln(k_{SC}/k_{CT})$	$\Phi_{SC}{}^{c}$	$\Phi_{free}{}^{d}$
unannealed P3HT:PCBM (1:1)	3.2	12	7.9	0.52	0.59
vapor-annealed P3HT:PCBM (1:1)	2.2	9.8	7.7	0.71	0.75
P3HT:PCBM (19:1)	1.5	3.6	8.4	0.8	–
vapor-annealed P3HT:PCBM (1:1, 355 nm exc.)	2.3	3.7	8.7	0.58	0.71
PCDTBT:PCBM (1:4)	0.5	7.4	6.5	0.73	0.72
PCDTBT:PCBM (19:1)	0.8	5.8	7.2	0.87	–
PCPDTBT: PCBM (1:2)	3.5	86	6.0	0.54	0.64
MEH-PPV: PCBM (1:1)	7.5	14	8.6	0.20	0.26
MEH-PPV: PCBM (1:4)	7.3	14	8.6	0.28	0.41

[a]The center of the Gaussian corresponding to the faster recombination phase at 10 K. [b]The center of the Gaussian corresponding to the slower recombination phase at 10 K. [c]Integrated decay amplitude in the slower Gaussian recombination phase. [d]Room temperature free charge yield obtained by applying the kinetic model in ref 9 to intensity-dependent recombination measurements (full data in Supporting Information).

dynamics. Alternative unconstrained rate distributions for each sample (Supporting Information) show the emergence of bimodal character, confirming that fitting to a well-parametrized bimodal rate distribution is appropriate. In all cases, the fast phase of recombination equates to bound CT lifetimes peaked at ∼2−20 ns and the slow phases reflect lifetimes peaked at ∼1−10 μs, with substantial width in the slower recombination phase.

Figure 5a shows that the yield of SCs (from the slow tunneling phase) is very strongly correlated with the yield of free charges extracted from intensity-dependent measurements across the series of samples with widely varying efficiencies. The least-squares regression line has a slope close to 1, and an intercept close to 0, which is strong evidence that our analysis of the two independent measurements is sufficiently well parametrized to derive insight into the properties of SCs. Yields of SCs/free charges (measured via both methods) are highest for blends of PCBM with either P3HT, PCPDTBT, or PCDTBT, followed by the unannealed P3HT blend, while MEH-PPV blends have the lowest free charge yields. This trend broadly correlates with photon-to-current quantum efficiencies previously measured for devices made from the same materials.[12,13,48,51,52]

Implications for Free Charge Photogeneration. The universal link we observe between yields of SCs and free charges leads us to the clear conclusion that populations of free (extractable) charges are established via long-range charge separation within the thermalization time scale, which is presumed to be substantially faster than the fastest recombination rates we resolve. Our data therefore strongly support models invoking branching between bound and free charge populations. Moreover, the bimodal distribution of recombination rates strongly implies the presence of an energetic barrier between CT states and SCs. Charge pairs are less likely to be found with an intermediate separation in our experiment because if they fall short of a critical separation within the thermalization time scale, they will instead collapse into tightly bound CT states that are identified by their subsequent recombination rate. The probability of overcoming this barrier
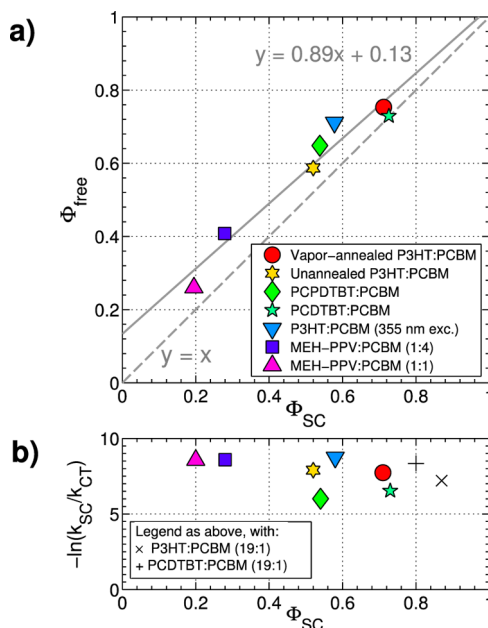
Figure 5. (a) Yield of SCs at 10 K (from the slower fitted Gaussian component) versus the yield of free charges measured via fitting the intensity-dependent recombination at room temperature to the kinetic model in ref 9. The linear regression fit is also shown, along with the $y = x$ line as a guide. The full set of intensity-dependent recombination at fits can be found in the Supporting Information. (b) Negative logarithm of the ratio of peak recombination rate constants, which is proportional to the charge pair separation of the SC population for a given tunneling attenuation constant, β.

within the thermalization time scale is therefore what defines the key branching step. Our fits already assumed a bimodal rate distribution, but we emphasize that this was justified based on the bimodal distributions that still emerged from unconstrained rate distributions (Figure 2, and the entire set of fits for other samples in the Supporting Information). The implication of branching during thermalization is at odds with Vandewal et al.,[22] who concluded that relaxed CT states can efficiently contribute to photocurrent generation. The two observations might be reconciled if the thermal barrier were easily overcome at room temperature; however, the strong correlation we observe between Φ_{SC} at low temperature and Φ_{free} at room temperature suggests this is not the case. It would be interesting to employ the present experiment to examine the charge pair distance distribution after directly exciting the relaxed CT state; however, its vanishingly small absorption cross-section precluded this measurement in the TA format. We note, however, that we refer to CT states here as the closest bound states, rather than using the formal definition that requires radiative coupling. It is possible that the electroluminescent subset of CT states probed in ref 22 may still have some degree of electron-hole separation/delocalization.

Before we consider the question of absolute distances, we can compare the relative charge separation distributions across the series of materials on the basis that $-\ln(k_{SC}/k_{CT})$ is proportional to charge pair separation (eq 3), where k_{SC} is the peak rate for SCs. Since each value of k_{SC} is referenced to the k_{CT} value measured for the same sample, the minor intrinsic rate variations between different materials is already accounted for (e.g., non-distance contributions to electronic coupling). These values are plotted in Figure 5b. Considering the wide range of charge separation efficiencies probed, overall we

observe very little variation in $-\ln(k_{SC}/k_{CT})$; the total range is only 35% of the mean value. This shows that SCs for different materials are all described by similar critical separations (assuming similar β values); variation in recombination dynamics reflects the relative probability that charge pairs achieved the critical separation for different materials.

By comparing selected pairs of samples, we can also look deeper within the universal correlation to identify the underlying reasons for variation. While comparing the efficiency of different blends is not a new strategy, we emphasize that here we are isolating the properties of the frozen primary charge pairs. In the case of the 1:1 P3HT:PCBM blends, we see that solvent vapor annealing translates to higher yields of SCs (*vide supra*) as a result of forming more crystalline phases of an optimum size.

In the case of MEH-PPV:PCBM blends, molecular PCBM is more readily dissolved throughout MEH-PPV since MEH-PPV is less crystalline than P3HT. Accordingly, optimized MEH-PPV:PCBM devices feature excess PCBM in order to create sufficiently large and interconnected PCBM phases. Although it is reasonable to assume that the need for excess PCBM relates to electron extraction, our comparison of 1:1 and 1:4 blends shows that excess PCBM results in higher yields of primary SCs. Consistent with a recent combined theoretical and experimental study by Savoie et al.,[53] the difference between the relative distance distributions for the MEH-PPV blends reflects the benefit of larger PCBM domains in the charge separation step.

By exciting the P3HT:PCBM blends at 355 nm as well as 532 nm, we were able to observe that direct PCBM excitation can also lead to comparably high SC yields. This result is consistent with other recent spectroscopic measurements[54] and spectrally resolved photocurrent measurements for devices at room temperature.

We also probed the relative roles of polymer and fullerene components in free charge photogeneration by carrying out measurements on films with only 5% PCBM blended with P3HT or PCDTBT (labeled as 19:1). The low PCBM content remains sufficient to achieve efficient initial charge photogeneration;[55] however, the small and isolated PCBM domains cannot play a significant role in creating SCs. When comparing the 19:1 blends with more fullerene-rich counterparts, surprisingly, we find that the creation of SCs is not suppressed by PCBM dilution. In fact, we observe a higher relative yield of SCs (compared with CTs) in the 19:1 blends for both P3HT and PCDTBT, noting that the total charge yield could be diminished due to exciton decay beforehand. This result does not contradict the established higher optimum PCBM content in devices because free charge photogeneration must be balanced with charge extraction requirements in devices. Limited electron diffusion in the 19:1 blends also means that free charge formation cannot be alternatively quantified via intensity-dependent recombination dynamics,[9] or by pump–push–probe photocurrent spectroscopy.[16] The tunneling recombination measurement is uniquely positioned to examine the intrinsic charge separation step in these dilute blends, and leads us to conclude that formation of SCs does not necessarily require large PCBM phases. Unlike the MEH-PPV blends discussed above, where PCBM crystals were crucial for charge separation, the blends with only 5% PCBM highlight the role of the polymers in achieving initial long-range charge separation. The higher yield of SCs for 19:1 blends may be attributed to more extensive and ordered pure polymer domains. Extended

polymer chains support highly delocalized excitons, which may couple to SC states prior to localizing.[20]

Charge Separation Length Scales. Finally, we address the question of absolute length scales by considering the tunneling attenuation factor, β. Most commonly formulated in a superexchange model, lower values of β result when the tunneling barrier is reduced.[46,47,56,57] In donor–bridge–acceptor model systems, β values as low as ~ 0.1 Å^{-1} have been measured when π-conjugated bridges with a small energy gap are used, thus contributing to electron tunneling over distances longer than 3 nm.[47] β values smaller than 0.6 Å^{-1} are considered reasonable for OPV blends, which inherently feature a dense set of low energy gap π-conjugated tunneling pathways.[25] We note that β for more commonly studied charge separation reactions is not the same as for charge recombination in the same photoinduced ET system: the former couples an excited state with a charge-separated state, while the latter returns the charge-separated state to the electronic ground state. Slightly higher β values have been measured for charge recombination in some donor–bridge–acceptor systems,[47] and it is tempting to assume that this must always be the case on account of the electron stabilization in the charge-separated state contributing to a higher tunneling barrier for charge recombination. However, it is important to realize that in the semi-classical ET formalism, electron tunneling is in fact dependent on the tunneling of *nuclear* coordinates. Since recombination couples charge-separated and ground-state surfaces (without involvement of the excited state that preceded charge separation), low β values for charge recombination in OPV films are still considered likely.

Caruso and Troisi calculated distributions of β for charge separation by modeling entire disordered polymer–fullerene heterojunctions over several nanometers.[25] They found broad distributions of $\beta \approx 0.2-0.6$ Å^{-1}. The observed range reflects the dependence on energetic disorder and the anisotropy. In the absence of a similar detailed study on β for charge recombination in the materials studied here, we apply this reasonable range of β values to transform our measured rate distributions into distance distributions.

Figure 6a shows the distance distribution of charge pairs for vapor annealed P3HT:PCBM. The plot is obtained by using eq 3 to transform the recombination rate constant distributions in Figure 3 onto a distance scale, using several plausible β values. k_{CT} is taken as the peak of the fast recombination phase, such that the x-axis represents the excess charge separation compared with CT states. For $\beta \approx 0.3-0.2$ Å^{-1}, the SCs have separations $\sim 2.5-4$ nm greater than those of CT states.

Figure 6b shows the distance corresponding to the peak of the SC population for all films as a function of β. The values were obtained by applying eq 3 to the ratio k_{SC}/k_{CT} taken from Table 1, which were derived from the fitted charge recombination curves in Figure 4. The tight clustering of the charge separation values reflects the similarity of the rate constants noted above and in Figure 5b. Since the SC yields were already shown to be correlated with free charge yields (Figure 5), the SC distances shown in Figure 6b represent critical charge separations that must be achieved within the thermalization time scale in order to generate free charges. Figure 6b shows that reasonably low values of β (0.3 Å^{-1}) consistently place the SC distances $\sim 2-3$ nm greater than those for CT states. Even the maximum β value of 0.6 Å^{-1} places SC distances ~ 1.5 nm greater than those for for CT states. Considering the range of measured $-\ln(k_{SC}/k_{CT})$ values,
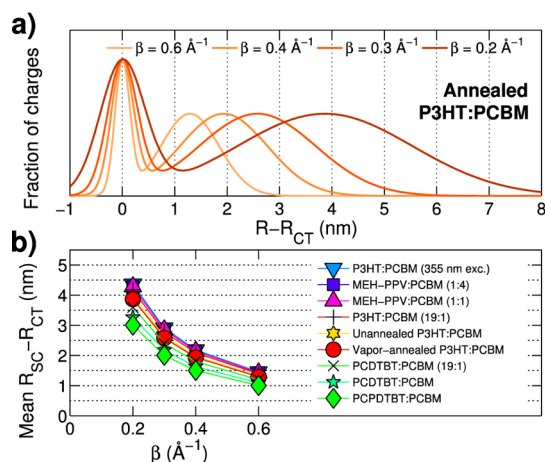
Figure 6. (a) Extracted distributions of charge pair distances for annealed P3HT:PCBM obtained by applying various values of β to the fitted tunneling rate constant distribution in Figure 3. (b) Mean charge pair distances as a function of β for the SC (slower recombining) populations of charges fitted for various blends in Figure 4.

of possible β values, and of CT separations, we estimate that free charges are defined by primary thermalized separations of ~3−4 nm. The absolute distance scale could be further refined by calculating distributions of β for charge recombination in these materials (along the lines of ref 25) and applying to the measured rate distributions.

CONCLUSIONS

We were able to access a regime at low temperature where photogenerated charge pairs are frozen at the separations at which they thermalize and slowly recombine via tunneling. By fitting tunneling recombination dynamics to a double Gaussian distribution of rate constants, we identified populations of CT states and SCs. We observed a universal link between the yield of initial SCs at low temperature and the yield of free charges identified by bimolecular charge recombination at room temperature. We therefore conclude that in OPV devices, populations of free (extractable) charges are established via long-range charge separation within the thermalization time scale. Subject to assumed values of $\beta \approx 0.3$ Å^{-1}, we estimate that initial charge separations of ~3−4 nm equate to free charges at room temperature in all material blends, and differences between materials are manifest in their branching ratios. Our measurements support the various branching models and augment them with spatial information. The bimodal recombination rate distribution, which also emerges from fits that do not presume its shape, provides evidence of an energetic barrier between populations of CTs and SCs. Correlation with room temperature free charge yields suggests that this barrier exceeds thermal energy at room temperature.

Because we recover information about primary charge pairs by freezing them and resolving their subsequent recombination, we are unable to time-resolve the distance coordinate of charge separation. Thus, we cannot distinguish between direct long-range charge separation (perhaps aided by delocalization) and rapid charge diffusion during thermalization. Nevertheless, the experiment and analysis we have developed provides an insightful probe of the properties of initial charge pairs. By resolving the effect of fullerene content in MEH-PPV blends, we found that charge separation yields were dependent on forming fullerene crystals. However, the important role of the

polymers was highlighted in blends that achieved significant charge separation with minimal fullerene. We found that SCs were also generated via fullerene photoexcitation. We expect the approach described to be of considerable value in guiding new material development and may form the basis of correlations against, for example, disorder parameters, CT excitation energy, quantum coherence, or delocalization lengths. By isolating distance distributions achieved in the primary charge separation step, tunneling recombination measurements are ideally positioned to test the validity of current and future models for long-range charge separation.

ASSOCIATED CONTENT

Ⓢ Supporting Information

Sample preparation details, temperature-dependent polarization anisotropy decay, visible and IR broadband TA spectra, and details of the fits used to determine Φ_{SC} and Φ_{free}. This material is available free of charge via the Internet at http://pubs.acs.org.

AUTHOR INFORMATION

Corresponding Author
justin.hodgkiss@vuw.ac.nz

Notes
The authors declare no competing financial interest.

ACKNOWLEDGMENTS

REFERENCES

(1) Clarke, T. M.; Durrant, J. R. *Chem. Rev.* **2010**, *110*, 6736−6767.
(2) Brédas, J.-L.; Norton, J. E.; Cornil, J.; Coropceanu, V. *Acc. Chem. Res.* **2009**, *42*, 1691−1699.
(3) Gregg, B. A.; Chen, S.-G.; Cormier, R. A. *Chem. Mater.* **2004**, *16*, 4586−4599.
(4) Morteani, A.; Sreearunothai, P.; Herz, L.; Friend, R.; Silva, C. *Phys. Rev. Lett.* **2004**, *92*, No. 247402.
(5) Offermans, T.; van Hal, P.; Meskers, S.; Koetse, M.; Janssen, R. *Phys. Rev. B* **2005**, *72*, No. 045213.
(6) Guo, J.; Ohkita, H.; Benten, H.; Ito, S. *J. Am. Chem. Soc.* **2010**, *132*, 6154−6164.
(7) Yin, C.; Kietzke, T.; Neher, D.; Hörhold, H.-H. *Appl. Phys. Lett.* **2007**, *90*, No. 092117.
(8) Zhou, Y.; Tvingstedt, K.; Zhang, F.; Du, C.; Ni, W.-X.; Andersson, M. R.; Inganäs, O. *Adv. Funct. Mater.* **2009**, *19*, 3293−3299.
(9) Howard, I. A.; Mauer, R.; Meister, M.; Laquai, F. *J. Am. Chem. Soc.* **2010**, *132*, 14866−14876.
(10) Westenhoff, S.; Howard, I. A.; Hodgkiss, J. M.; Kirov, K. R.; Bronstein, H. A.; Williams, C. K.; Greenham, N. C.; Friend, R. H. *J. Am. Chem. Soc.* **2008**, *130*, 13653−13658.
(11) Hodgkiss, J. M.; Campbell, A. R.; Marsh, R. A.; Rao, A.; Albert-Seifried, S.; Friend, R. H. *Phys. Rev. Lett.* **2010**, *104*, No. 177701.
(12) Ma, W.; Yang, C.; Gong, X.; Lee, K.; Heeger, A. J. *Adv. Funct. Mater.* **2005**, *15*, 1617−1622.
(13) Peet, J.; Kim, J. Y.; Coates, N. E.; Ma, W. L.; Moses, D.; Heeger, A. J.; Bazan, G. C. *Nat. Mater.* **2007**, *6*, 497−500.
(14) Marsh, R. A.; Hodgkiss, J. M.; Albert-Seifried, S.; Friend, R. H. *Nano Lett.* **2010**, *10*, 923−930.
(15) Campbell, A. R.; Hodgkiss, J. M.; Westenhoff, S.; Howard, I. A.; Marsh, R. A.; McNeill, C. R.; Friend, R. H.; Greenham, N. C. *Nano Lett.* **2008**, *8*, 3942−3947.

(16) Bakulin, A. A.; Rao, A.; Pavelyev, V. G.; van Loosdrecht, P. H. M.; Pshenichnikov, M. S.; Niedzialek, D.; Cornil, J.; Beljonne, D.; Friend, R. H. *Science* **2012**, *335*, 1340−1344.

(17) Gelinas, S.; Rao, A.; Kumar, A.; Smith, S. L.; Chin, A. W.; Clark, J.; van der Poll, T. S.; Bazan, G. C.; Friend, R. H. *Science* **2014**, *343*, 512−516.

(18) Grancini, G.; Maiuri, M.; Fazzi, D.; Petrozza, A.; Egelhaaf, H.-J.; Brida, D.; Cerullo, G.; Lanzani, G. *Nat. Mater.* **2013**, *11*, 29−33.

(19) Jailaubekov, A. E.; Willard, A. P.; Tritsch, J. R.; Chan, W.-L.; Sai, N.; Gearba, R.; Kaake, L. G.; Williams, K. J.; Leung, K.; Rossky, P. J.; Zhu, X.-Y. *Nat. Mater.* **2013**, *12*, 66−73.

(20) Chen, K.; Barker, A. J.; Reish, M. E.; Gordon, K. C.; Hodgkiss, J. M. *J. Am. Chem. Soc.* **2013**, *135*, 18502−18512.

(21) Lee, J.; Vandewal, K.; Yost, S. R.; Bahlke, M. E.; Goris, L.; Baldo, M. A.; Manca, J. V.; Voorhis, T. V. *J. Am. Chem. Soc.* **2010**, *132*, 11878−11880.

(22) Vandewal, K.; Albrecht, S.; Hoke, E. T.; Graham, K. R.; Widmer, J.; Douglas, J. D.; Schubert, M.; Mateker, W. R.; Bloking, J. T.; Burkhard, G. F.; Sellinger, A.; Fréchet, J. M. J.; Amassian, A.; Riede, M. K.; McGehee, M. D.; Neher, D.; Salleo, A. *Nat. Mater.* **2013**, *13*, 63−68.

(23) van Eersel, H.; Janssen, R. A. J.; Kemerink, M. *Adv. Funct. Mater.* **2012**, *22*, 2700−2708.

(24) Howard, I. A.; Etzold, F.; Laquai, F.; Kemerink, M. *Adv. Energy Mater.* **2014**, *4*, 1301743.

(25) Caruso, D.; Troisi, A. *Proc. Natl. Acad. Sci. U.S.A.* **2012**, *109*, 13498−13502.

(26) Jarzab, D.; Cordella, F.; Gao, J.; Scharber, M.; Egelhaaf, H.-J.; Loi, M. A. *Adv. Energy Mater.* **2011**, *1*, 604−609.

(27) Veldman, D.; İpek, Ö.; Meskers, S. C. J.; Sweelssen, J.; Koetse, M. M.; Veenstra, S. C.; Kroon, J. M.; Bavel, S. S. V.; Loos, J.; Janssen, R. A. J. *J. Am. Chem. Soc.* **2008**, *130*, 7721−7735.

(28) Huang, Y.-S.; Westenhoff, S.; Avilov, I.; Sreearunothai, P.; Hodgkiss, J. M.; Deleener, C.; Friend, R. H.; Beljonne, D. *Nat. Mater.* **2008**, *7*, 483−489.

(29) Taguchi, D.; Shino, T.; Zhang, L.; Li, J.; Weis, M.; Manaka, T.; Iwamoto, M. *Appl. Phys. Express* **2011**, *4*, No. 021602.

(30) Kaake, L. G.; Jailaubekov, A.; Williams, K. J.; Zhu, X.-Y. *Appl. Phys. Lett.* **2011**, *99*, No. 083307.

(31) Meister, M.; Baumeier, B.; Pschirer, N.; Sens, R.; Bruder, I.; Laquai, F.; Andrienko, D.; Howard, I. A. *J. Phys. Chem. C* **2013**, *117*, 9171−9177.

(32) Chepelianskii, A. D.; Wang, J.; Friend, R. H. *Phys. Rev. Lett.* **2014**, *112*, No. 126802.

(33) Paquin, F.; Latini, G.; Sakowicz, M.; Karsenti, P.-L.; Wang, L.; Beljonne, D.; Stingelin, N.; Silva, C. *Phys. Rev. Lett.* **2011**, *106*, 197401−197404.

(34) Mikhnenko, O. V.; Cordella, F.; Sieval, A. B.; Hummelen, J. C.; Blom, P. W. M.; Loi, M. A. *J. Phys. Chem. B* **2008**, *112*, 11601−11604.

(35) Grzegorczyk, W. J.; Savenije, T. J.; Dykstra, T. E.; Piris, J.; Schins, J. M.; Siebbeles, L. D. A. *J. Phys. Chem. C* **2010**, *114*, 5182−5186.

(36) Piris, J.; Dykstra, T. E.; Bakulin, A. A.; Loosdrecht, P. H. M. V.; Knulst, W.; Trinh, M. T.; Schins, J. M.; Siebbeles, L. D. A. *J. Phys. Chem. C* **2009**, *113*, 14500−14506.

(37) Guo, J.; Ohkita, H.; Benten, H.; Ito, S. *J. Am. Chem. Soc.* **2009**, *131*, 16869−16880.

(38) Kraabel, B.; Moses, D.; Heeger, A. J. *J. Chem. Phys.* **1995**, *103*, 5102.

(39) Busby, E.; Carroll, E. C.; Chinn, E. M.; Chang, L.; Moulé, A. J.; Larsen, D. S. *J. Phys. Chem. Lett.* **2011**, *2*, 2764−2769.

(40) Shuttle, C. G.; Hamilton, R.; O'Regan, B. C.; Nelson, J.; Durrant, J. R. *Proc. Natl. Acad. Sci. U.S.A.* **2010**, *107*, 16448−16452.

(41) Mauer, R.; Howard, I. A.; Laquai, F. *J. Phys. Chem. Lett.* **2010**, *1*, 3500−3505.

(42) De Vault, D.; Chance, B. *Biophys. J.* **1966**, *6*, 825−847.

(43) DeVault, D.; Parkes, J. H.; Chance, B. *Nature* **1967**, *215*, 642−644.

(44) Jortner, J. *J. Chem. Phys.* **1976**, *64*, 4860.

(45) Hopfield, J. J. *Proc. Natl. Acad. Sci. U.S.A.* **1974**, *71*, 3640−3644.

(46) Gray, H. B.; Winkler, J. R. *Chem. Phys. Lett.* **2009**, *483*, 1−9.

(47) Albinsson, B.; Martensson, J. *J. Photochem. Photobiol. C: Photochem. Rev.* **2008**, *9*, 138−155.

(48) Zhao, Y.; Xie, Z.; Qu, Y.; Geng, Y.; Wang, L. *Appl. Phys. Lett.* **2007**, *90*, No. 043504.

(49) Di Nuzzo, D.; Aguirre, A.; Shahid, M.; Gevaerts, V. S.; Meskers, S. C. J.; Janssen, R. A. J. *Adv. Mater.* **2010**, *22*, 4321−4324.

(50) Etzold, F.; Howard, I. A.; Forler, N.; Cho, D. M.; Meister, M.; Mangold, H.; Shu, J.; Hansen, M. R.; Müllen, K.; Laquai, F. *J. Am. Chem. Soc.* **2012**, *134*, 10569−10583.

(51) Yu, G.; Gao, J.; Hummelen, J. C.; Wudl, F.; Heeger, A. J. *Science* **1995**, *270*, 1789−1791.

(52) Park, S. H.; Roy, A.; Beaupre, S.; Cho, S.; Coates, N.; Moon, J. S.; Moses, D.; Leclerc, M.; Lee, K.; Heeger, A. J. *Nat. Photon.* **2009**, *3*, 297−302.

(53) Savoie, B. M.; Rao, A.; Bakulin, A. A.; Gélinas, S.; Movaghar, B.; Friend, R. H.; Marks, T. J.; Ratner, M. A. *J. Am. Chem. Soc.* **2014**, *136*, 2876−2884.

(54) Paraecattil, A. A.; Banerji, N. *J. Am. Chem. Soc.* **2014**, *136*, 1472−1482.

(55) Ohkita, H.; Cook, S.; Astuti, Y.; Duffy, W.; Tierney, S.; Zhang, W.; Heeney, M.; McCulloch, I.; Nelson, J.; Bradley, D. D. C.; Durrant, J. R. *J. Am. Chem. Soc.* **2008**, *130*, 3030−3042.

(56) McConnell, H. M. *J. Chem. Phys.* **1961**, *35*, 508.

(57) Beratan, D. N.; Betts, J. N.; Onuchic, J. N. *Science* **1991**, *252*, 1285−1288.

12026

dx.doi.org/10.1021/ja505380j | *J. Am. Chem. Soc.* 2014, 136, 12018−12026